Convective mixing in homogeneous porous media flow

Jia-Hau Ching,[1,2] Peilong Chen,[2] and Peichun Amy Tsai[1,*]
[1]*Department of Mechanical Engineering, University of Alberta, Edmonton, Alberta T6G 2G8, Canada*
[2]*Department of Physics, National Central University, Zhongli 320, Taiwan*
(Received 21 July 2016; published 31 January 2017)

Inspired by the flow processes in the technology of carbon dioxide (CO_2) storage in saline formations, we modeled a homogeneous porous media flow in a Hele-Shaw cell to investigate density-driven convection due to dissolution. We used an analogy of the fluid system to mimic the diffusion and subsequent convection when CO_2 dissolves in brine, which generates a heavier solution. By varying the permeability, we examined the onset of convection, the falling dynamics, the wavelengths of fingers, and the rate of dissolution, for the Rayleigh number Ra (a dimensionless forcing term which is the ratio of buoyancy to diffusivity) in the range of $2.0 \times 10^4 \leqslant \mathrm{Ra} \leqslant 8.26 \times 10^5$. Our results reveal that the effect of permeability influences significantly the initial convective speed, as well as the later coarsening dynamics of the heavier fingering plumes. However, the total dissolved mass, characterized by a nondimensional Nusselt number Nu, has an insignificant dependence on Ra. This implies that the total dissolution rate of CO_2 is nearly constant in high Ra geological porous structures.

DOI: 10.1103/PhysRevFluids.2.014102

I. INTRODUCTION

Convective mixing, in contrast to slow diffusion, significantly enhances the transport of mass, heat, and energy. The process plays a central role in industrial processes, oceanic and atmospheric circulations, as well as stellar systems [1]. The mixing process is also crucial for successful carbon capture and sequestration (CCS) technology [2,3], with which CO_2 is collected and stored in underground, brine-saturated, porous media (e.g., the ongoing Sleipner [4,5] and Salah Projects [6,7]). CO_2 is injected into a high-pressure and high-temperature saline aquifer. During this process, CO_2 is in a supercritical state [8], rises to the top (due to its low density of 500–800 $\mathrm{kg/m^3}$), and is stopped by impermeable cap-rock formation [8–10]. Over time, CO_2 dissolves into the brine via diffusion, creating a denser CO_2-brine mixture than either of the pure fluids [9]. When this diffusion layer becomes sufficiently thick, convection sets in due to unstable gravitational and stratified flows, increasing the transport and storage of CO_2.

Accurate predictions and measurements of convection-enhanced dissolution rates are extremely important for the CCS technology. As a result they have recently been studied using theory, simulations [11–14], and experiments [15–18]. Analytical and numerical calculations have been performed to predict the onset of this out-of-equilibrium, dissolution-driven convection, which occurs above a critical nondimensional forcing term, described by the Rayleigh number, Ra [19–24]. The convection precipitates the downward motion of the CO_2-rich brine, thereby crucially reducing the horizontal spreading of the initially buoyant CO_2 [25–27].

However, it is challenging to perform laboratory experiments for supercritical CO_2, which requires the surrounding pressure to be $\geqslant$100 bar. Several innovative fluid systems, with either binary fluids or one-side dissolution systems, have been adopted to mimic and generate density-driven convection of CO_2-brine mixture at the standard atmospheric condition [15–17,28,29]. Nevertheless,

*peichun.amy.tsai@ualberta.ca

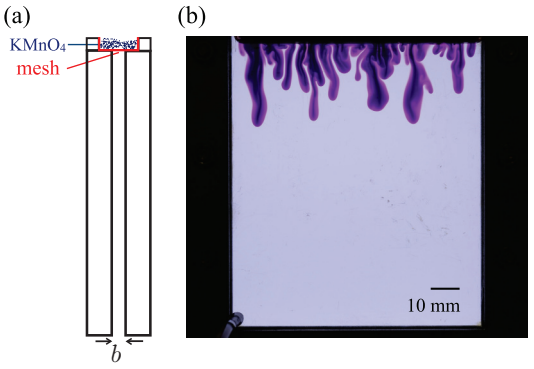

FIG. 1. Experimental diagrams: (a) side view of the Hele-Shaw cell, consisting of two parallel plates with an uniform gap thickness, b; (b) a snapshot of the front view of density-driven fingering due to the heavier mixture of $KMnO_4$ dissolution into water in a Hele-Shaw cell as a homogeneous porous medium.

the dependence of enhanced convective flux on the Nusselt (Nu), or Sherwood (Sh), number is still unresolved; some numerical and experimental studies [15,16,28,30,31] reveal Nu-Ra scaling laws, whereas other recent work [11–14,29] show the dissolution flux is independent of Ra (for $10^3 \lesssim \mathrm{Ra} \lesssim 10^5$ [11,12]). Therefore, a primary object of our systematic experiments was to examine the Nu-Ra relation, which provides important implications for the CCS capacity and process.

II. EXPERIMENTAL

To successfully mimic CO_2 dissolution in a saline aquifer, an experimental design was chosen according to the following criteria: greater mixture density, clear visualization, and accurate and measurable mixture concentration and density. Inspired by a previous study [17], potassium permanganate ($KMnO_4$) and water were used to mimic the mixing process of CO_2 into brine. The resulting density increased ($\Delta\rho = 46$ kg m^{-3} at 25 °C [32]) and saturated mass fraction of $KMnO_4$ to water ($w_{\mathrm{sat}} = 0.067$) were comparable to the mixing condition of CO_2 into brine (with $\Delta\rho$ and w_{sat} up to 30 kg m^{-3} and 0.07, respectively, at reservoir conditions [33]). Similar to the change of the liquid density for CO_2 dissolved in saline, $\Delta\rho$ linearly increased with the dissolution concentration, w. The mixture of water and $KMnO_4$ gives a vivid (purple) color, which is related to transmitted light intensity and can be calibrated to obtain accurate concentration of dissolved $KMnO_4$. A previous study using this fluid system focused on low Ra-number flow ($\leqslant$1700) by using an inclined Hele-Shaw plate to investigate the dissolution processes and the transition from diffusion to convection [17]. In this work, we focus on the mixing processes and total dissolution rates in the high-Ra region ($10^4 < \mathrm{Ra} < 10^6$), by using different permeabilities, k.

Figure 1 shows our experimental setup of homogeneous porous media flow, modeled by a Hele-Shaw cell (with the cell height of 126 mm). The cell consists of two parallel polycarbonate plates, separated by a stainless steel shim. The thickness of the shim, b, controls the permeability of the porous medium, k, via Darcy's relationship of $k = b^2/12$ for homogeneous porous media [34]. We varied b from 80 to 515 μm and, as a result, obtained the permeability range of $5.33 \times 10^{-10} \leqslant k \leqslant 2.21 \times 10^{-8}$ m^2. To mimic the density-driven convection of the CCS process, initially $KMnO_4$ (1 g) powders were distributed uniformly on the top of the cell and held by a stainless steel mesh of nominal pore size of 43 μm (in a space of $5 \times 6 \times 11.24$ cm^3). We used a syringe pump to inject water at a steady rate (at 40 ml/min) from the bottom to ensure the water contacted the solute uniformly [see Fig. 1(a)]. During the experiments, the denser mixture was generated, and we measured the mixture concentration, mixing dynamics, and resulting convection [as shown in Fig. 1(b)].

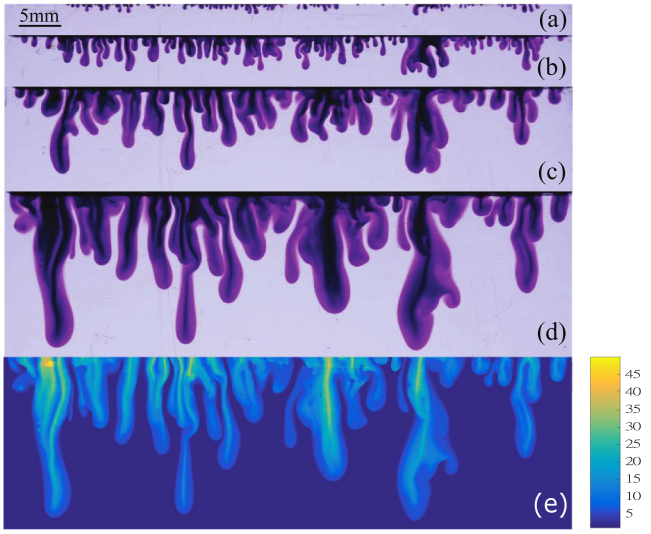

FIG. 2. (See the movies in the Supplemental Material [35].) Falling dynamics of heavier dissolution fingers in $b = 385\ \mu$m, Ra $= 4.6 \times 10^5$ at time (a) 9.85 s, (b) 12.42 s, (c) 19 s, and (d) 27.28 s, after the water contacted mesh. (e) Concentration distribution of the snapshot (d); the color bar shows the magnitude of the (weight) concentration, C_w [kg/m^3].

To obtain the local concentration of solute in the mixture $C_w = \rho(w)w$, where C_w is (weight) concentration (kg/m^3), $\rho(w)$ is mixture density (kg/m^3), and w is the mass fraction of solute to the solution, we carried out several calibrations relating the transmitted light intensity to the mass fraction w. Calibration curves were carried out for several mass fractions, which varied from 7.4×10^{-4} to 5.7×10^{-2}. We obtained the fitting formulas with least-square fits and checked the reliability and precision by comparing the concentration obtained from our fitting formulas with existing data [32]. This method enabled us to choose suitable color channels to accurately analyze the mixture concentration data. Different shim sizes, b, can slightly change the light intensity recorded, and this type of error is controlled within 5%.

III. RESULTS AND DISCUSSION

Once the solute is dissolved in water, a heavier mixture layer forms, which is gravitationally unstable. Within a few seconds, a number of dissolution bulbs formed at the interface. Figure 2 shows the convective dynamics of the heavier mixture. Initially, several bumps form at the interface and sink vertically, while expanding horizontally into a fingering shape. These initial fingers grow independently, as shown in Figs. 2(a) and 2(b). When the fingers are broad enough to collide with each other, they merge into larger fingers [see Fig. 2(c)]. Due to the merging process, the finger number gradually decreases [Fig. 2(d)]. The concentration of dissolution can be calculated from these snapshots and with our calibration data; for example, Fig. 2(e) is the concentration profile of the dissolution fingers in Fig. 2(d).

In general, we observed two ways of mixing, described below and shown in a movie in the Supplemental Material [35]. First, while heavier fingers move downward, the tips of the fingers begin to touch. This in turn closes the path of ascending water between the fingers. As a result, the ascending fresh solution moves along the outer boundary of the combined fingers and makes the finger roots merge. This usually happens for multiple fingers in a solution of strong concentration. The second route is that fingers with light concentration, or density, tend to move laterally due to the buoyant force exerted by rising fresh solution. These lighter, unsaturated fingers fall slowly and

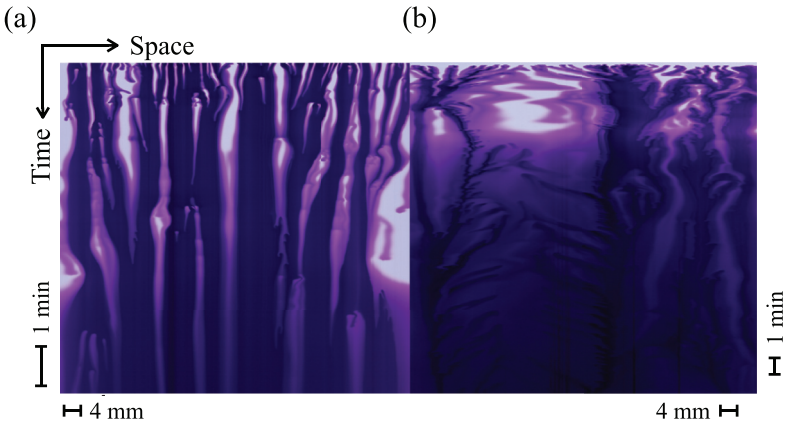

FIG. 3. Space-time diagrams of dense fingers revealing coarsening dynamics, for different permeabilities $k = 1.41 \times 10^{-9}$ m^2 in panel (a) and $k = 1.24 \times 10^{-8}$ m^2 in panel (b). Fingers are recorded at 1.5 mm below the interface where the dissolution takes place.

sometimes with lateral and upward movements, thereby bringing fresh water to the interface. These merging processes result in a decrease in the number of fingers, along with their coarsening. The development of fewer, wider fingers is shown in Fig. 3. We selected a plane below the interface (about 1.5 mm) to track the plume width and show the coarsening. In addition to the coarsening process, some newborn fingers combined with the heavier fingers which were formed earlier, instead of creating new routes, as might be expected.

Figure 3 also shows the effect of permeability on the coarsening dynamics: the greater the permeability, the faster the coarsening process of the dense fingers. To analyze this dependence quantitatively, we estimated the average wavelength of the fingers, $\langle\lambda\rangle$, which is the average distance between the fingers. Figure 4 reveals the wavelength evolution for different gap thicknesses. We calculated the finger wavelength with the number of dense fingers appearing at 1.5 mm below the

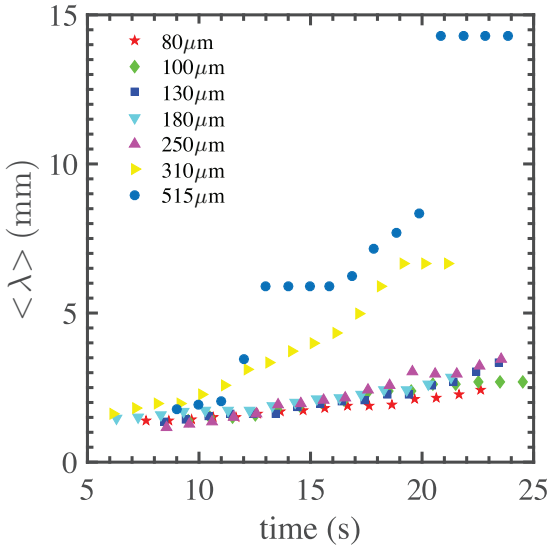

FIG. 4. Average wavelength $\langle\lambda\rangle$ evolution for different permeability k, revealing an insignificant variation of $\langle\lambda\rangle$ for small k (between 5.33×10^{-10} and 5.21×10^{-9} m^2), with $b = 80$–$250\,\mu$m.

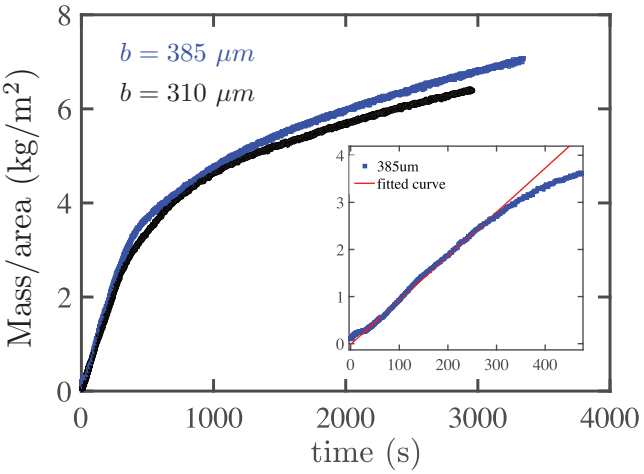

FIG. 5. Time evolution of total dissolution flux for two different permeabilities $k = 8.01 \times 10^{-9}$ and 1.24×10^{-8} m^2 (for $b = 310$ and 385 μm, respectively). The inset shows the best linear fit in the early time (before a full saturation).

interface. When the fingers are just formed, the average wavelength of the initial fingers for different k are nearly the same. We think this can be attributed to the similar initial dissolution process that is limited by the pore size of mesh holding the solute. However, while the fingers are falling, the wavelength for large k increases faster than that for small k.

Figure 5 reveals the evolution of dissolved mass flux calculated via $m/A = \int C_w dv/A$ [36], where A is the cross section area of the interface. In the early period, the total dissolution mass increases linearly with time. Once the whole cell is saturated with the dissolution (e.g., t $\approx$ 400 s in Fig. 5), the mass flux gradually decreases, resulting in a lower value of the slope at a later time. It is interesting to note that the decreasing of mass dissolution rate is due to a full saturation of the liquid cell, not a boundary effect when the descending plumes reach the bottom of the cell. The inset in Fig. 5 shows the best linear fit of the mass flux of dissolution in the early time and is used to estimate Nu.

The key objective of our experiments was to examine how density-driven convection enhances the dissolution rate of CO_2 for a wide range of Ra. We defined the dimensionless set as follows: $\mathrm{Ra} = \Delta\rho g k H/\mu D$, where $\Delta\rho$ is the maximal density difference between the saturated mixture and the original solution [32], μ is liquid viscosity (in our case, water viscosity $\mu = 9.2 \times 10^{-4}$ Pa s at 23 °C), g is the gravity coefficient, ϕ is the porosity, H is the height of the cell, and D is the diffusion coefficient of the solute ($D = 1.65 \times 10^{-9}$ m^2 s^{-1} for $KMnO_4$ [17]). Nusselt number Nu, a dimensionless mass flux is adopted to describe the dissolution rate of CO_2. $\mathrm{Nu} = F/(\phi\Delta\rho D/H)$ [2,15], where F is the mass flux and H is the height of the cell. For a homogeneous Hele-Shaw flow ($\phi = 1$), Nu can be simplified with the mass ratio of convective to diffusive processes, $\mathrm{Nu} = \phi V H/D$ [16,28], where V is the interfacial speed of the mixture.

We estimate the initial convective speed of the plumes, V_I, and hence the initial Nusselt number, Nu_I, by tracing the plume dynamics and the positions of finger tips of (at least) ten random fingers for each experiments. Figure 6(a) shows that within 180 s after the onset of convection, V_I increases with b, before the lead finger contacts the bottom boundary of the cell. A different Ra is obtained by varying the gap width, b (i.e., by changing the permeability, k). Due to both falling and ascending fingers, the data of V_I is scattered, resulting in a large deviation [as shown in Fig. 6(a)]. Figure 6(b) shows the best fit for early-time measurements of the Nu_I-Ra scaling law, $\mathrm{Nu}_I = \alpha \mathrm{Ra}^{\beta}$. By analyzing the early-time plume dynamics, we observe a weakly dependent scaling law with $\alpha = 587.1$, $\beta = 0.35$ in the early time. However, in time the descending plumes

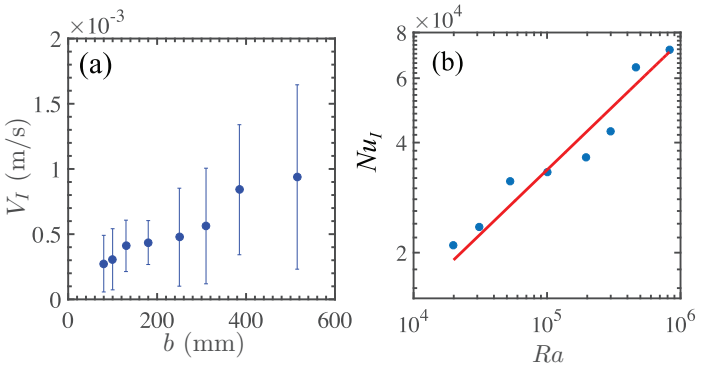

FIG. 6. (a) Early-time traveling speed V_I of falling plumes as a function of gap width b. (b) Early-time dimensionless convective mass flux, Nu_I, as a function of Ra. The solid line is the best power-law fitting of the form of $\mathrm{Nu}_I = \alpha \mathrm{Ra}^{\beta}$, with $\beta = 0.35$.

with lateral movement and diffusion start to interact and merge with neighbor plumes. These plume dynamics and interactions are manifested in a lateral diffusive flux [see Fig. 2(e)], then a coarsening of the space-time diagram of the plumes (i.e., Fig. 3), a decrease in the plume number at the top (solute-fluid) interface with time, and finally a slowing-down speed ($\approx$65% of V_I) in a later time. These observations agree with recent high-resolution results of plume dynamics obtained with shadowgraph imaging technique and different working fluids [29].

To accurately estimate the dimensionless total dissolution Nu, we further analyze the whole concentration field [using Fig. 2(e) snapshots and Fig. 5] and measured the mass-flux evolution of $KMnO_4$-water mixture before a full solute-saturation. Figure 7 shows the Nu-Ra relation, where Nu is calculated by linear fitting of mass flux F, obtained via $F = \dot{m}/A = \frac{\int C_w dv/A}{dt}$ from the early time measurement (e.g., Fig. 5 inset). Figure 7 shows the dimensionless dissolution flux for a wide range of Ra. For each Ra, we conducted three independent experiments to obtain the dissolution rate. The insignificant dependence on Ra implies that the dissolution mass flux is independent of Ra at high-Ra number. This experimental finding, using a fluid system with a linearly increase $\Delta\rho$ with C_w, agrees well with previous numerical results [12]. Several previous studies, however,

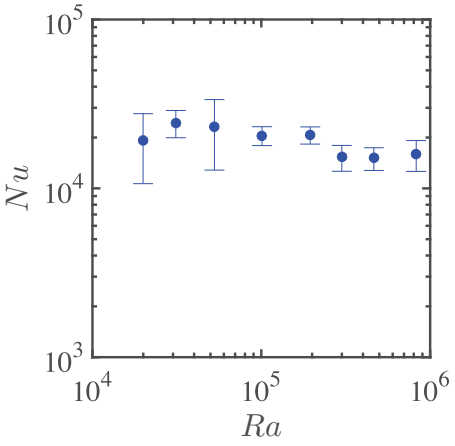

FIG. 7. The dimensionless dissolution flux, calculated using the linear growth rate of dissolution mass (e.g., Fig. 5 inset).

using different (binary) fluid systems of different $\Delta\rho(C_w)$ relations, reveal different scaling-law relation ($\mathrm{Nu} \sim \mathrm{Ra}^{\gamma}$, $\gamma \approx 0.75$–0.85 for $\mathrm{Ra} = 10^3$–10^6) [15,16,28]. In those experiments, when one liquid slowly dissolves into another, the liquid-liquid interface moves upwards evenly and the interfacial speed, V, and hence Nu, was estimated. In addition, these experiments use fluids with different trends of $\Delta\rho(C_w)$ from that of CO_2-brine dissolution. The dependence of liquid density on dissolution concentration, $\Delta\rho = f(C_w)$, varies for different fluid systems and significantly affects the Nu-Ra relationship, as demonstrated by a numerical study [12].

For our experimental system using one-side dissolution with a similar trend of $\Delta\rho$ as for the CO_2-brine system, the dissolution concentration profiles can be accurately obtained by taking into account the whole concentration field. The dissolution of the powder into liquid reveals a nearly constant and significant dissolution, or mass flux, $\langle \mathrm{Nu} \rangle \approx 1.9 \times 10^4$, in the high-Ra region. Furthermore, a recent study which uses a binary fluid system with high-resolution shadowgraphic visualization also demonstrates the independent relation between dissolution mass flux Nu and Ra [29]. The comparison of our result with previous numerical and experimental results (using different liquid systems) reveals an important role of the trend of $\Delta\rho(C_w)$ in the Nu-Ra relation.

IV. CONCLUSION

In summary, our experiments provide clear visualization and accurate measurements of the concentration field of dissolution flux in density-driven convection for homogeneous porous media in the high-Ra regime. We systematically investigated the convective fingering dynamics for different permeabilities; we found similar average wavelengths for small permeability and pronounced coarsening of heavier plumes for high permeability $k > 5.21 \times 10^{-9}$ m^2. In the high-Ra regime of $10^4 \lesssim \mathrm{Ra} \lesssim 10^6$, the data of solute concentration reveals large values of total dissolution flux, $\gtrsim 10^4$ times greater than diffusive mass flux due to convection. The results also show an insignificant dependence of the dimensionless dissolution flux, Nu, on Ra for high Ra, in agreement with previous numerical and experimental findings. It implies that, for a monotonic increasing density with dissolution concentration, the permeability of the geometrical structure plays a minor role in the total dissolution rate in high Ra number when CO_2 dissolves into brine. We also investigated the flow dynamics in this Ra region by examining the speed of fingering and the coarsening phenomenon. The fact that the average speed of the fingers increases and finger numbers decrease with increasing Ra provides an explanation for the independence in the Nu-Ra relation. Our results, with the comparison with previous studies, show that increasing density, as a function of solute concentration, plays a significant role in the enhancement of density-driven convection and total dissolution.

ACKNOWLEDGMENTS

P.A.T. acknowledges Natural Sciences and Engineering Research Council of Canada (NSERC) for the Discovery and Accelerator grants as well as Canada Research Chair Program in Fluids and Interfaces.

[1] G. Ahlers, S. Grossmann, and D. Lohse, Heat transfer and large scale dynamics in turbulent Rayleigh-Bénard convection, Rev. Mod. Phys. **81**, 503 (2009).

[2] H. E. Huppert and J. A. Neufeld, The fluid mechanics of carbon dioxide sequestration, Annu. Rev. Fluid Mech. **46**, 255 (2014).

[3] F. M. Orr *et al.*, Onshore geologic storage of CO_2, Science **325**, 1656 (2009).

[4] R. Korbøl and A. Kaddour, Sleipner vest CO_2 disposal-injection of removed CO_2 into the utsira formation, Energy Convers. Manage. **36**, 509 (1995).

[5] S. Lyle, H. E. Huppert, M. Hallworth, M. Bickle, and A. Chadwick, Axisymmetric gravity currents in a porous medium, J. Fluid Mech. **543**, 293 (2005).
[6] J. Rutqvist, D. W. Vasco, and L. Myer, Coupled reservoir-geomechanical analysis of CO_2 injection and ground deformations at in Salah, Algeria, Int. J. Greenh. Gas Control **4**, 225 (2010).
[7] A. Rucci, D. W. Vasco, and F. Novali, Monitoring the geologic storage of carbon dioxide using multicomponent SAR interferometry, Geophys. J. Int. **193**, 197 (2013).
[8] J. M. Nordbotten, M. A. Celia, and S. Bachu, Injection and storage of CO_2 in deep saline aquifers: Analytical solution for CO_2 plume evolution during injection, Transport Porous Med. **58**, 339 (2005).
[9] B. Metz *et al.*, *IPCC Special Report on Carbon Dioxide Capture and Storage* (Cambridge University Press, Cambridge, UK, 2005).
[10] S. Bachu and J. J. Adams, Sequestration of CO_2 in geological media in response to climate change: Capacity of deep saline aquifers to sequester CO_2 in solution, Energy Convers. Manage. **44**, 3151 (2003).
[11] M. L. Szulczewski, M. A. Hesse, and R. Juanes, Carbon dioxide dissolution in structural and stratigraphic traps, J. Fluid Mech. **736**, 287 (2013).
[12] J. J. Hidalgo, J. Fe, L. Cueto-Felgueroso, and R. Juanes, Scaling of Convective Mixing in Porous Media, Phys. Rev. Lett. **109**, 264503 (2012).
[13] G. S. H. Pau, J. B. Bell, K. Pruess, A. S. Almgren, M. J. Lijewski, and K. Zhang, High-resolution simulation and characterization of density-driven flow in CO_2 storage in saline aquifers, Adv. Water Resour. **33**, 443 (2010).
[14] A. C. Slim, Solutal-convection regimes in a two-dimensional porous medium, J. Fluid Mech. **741**, 461 (2014).
[15] J. A. Neufeld, M. A. Hesse, A. Riaz, M. A. Hallworth, H. A. Tchelepi, and H. E. Huppert, Convective dissolution of carbon dioxide in saline aquifers, Geophys. Res. Lett. **37**, L22404 (2010).
[16] S. Backhaus, K. Turitsyn, and R. E. Ecke, Convective Instability and Mass Transport of Diffusion Layers in a Hele-Shaw Geometry, Phys. Rev. Lett. **106**, 104501 (2011).
[17] A. C. Slim, M. M. Bandi, J. C. Miller, and L. Mahadevan, Dissolution-driven convection in a Hele-Shaw cell, Phys. Fluids **25**, 024101 (2013).
[18] T. J. Kneafsey and K. Pruess, Laboratory flow experiments for visualizing carbon dioxide-induced, density-driven brine convection, Transport Porous Med. **82**, 123 (2010).
[19] J. Ennis-King, I. Preston, and L. Paterson, Onset of convection in anisotropic porous media subject to a rapid change in boundary conditions, Phys. Fluids **17**, 084107 (2005).
[20] A. C. Slim and T. S. Ramakrishnan, Onset and cessation of time-dependent, dissolution-driven convection in porous media, Phys. Fluids **22**, 124103 (2010).
[21] A. Riaz, M. Hesse, H. A. Tchelepi, and F. M. Orr, Onset of convection in a gravitationally unstable diffusive boundary layer in porous media, J. Fluid Mech. **548**, 87 (2006).
[22] X. Xu, S. Chen, and D. Zhang, Convective stability analysis of the long-term storage of carbon dioxide in deep saline aquifers, Adv. Water Resour. **29**, 397 (2006).
[23] S. Rapaka, S. Chen, R. J. Pawar, P. H. Stauffer, and D. Zhang, Non-modal growth of perturbations in density-driven convection in porous media, J. Fluid Mech. **609**, 285 (2008).
[24] S. Rapaka, R. J. Pawar, P. H. Stauffer, D. Zhang, and S. Chen, Onset of convection over a transient base-state in anisotropic and layered porous media, J. Fluid Mech. **641**, 227 (2009).
[25] D. Pritchard, A. W. Woods, and A. J. Hogg, On the slow draining of a gravity current moving through a layered permeable medium, J. Fluid Mech. **444**, 23 (2001).
[26] C. W. MacMinn, J. A. Neufeld, M. A. Hesse, and H. E. Huppert, Spreading and convective dissolution of carbon dioxide in vertically confined, horizontal aquifers, Water Resour. Res. **48**, W11516 (2012).
[27] C. W. MacMinn and R. Juanes, Buoyant currents arrested by convective dissolution, Geophys. Res. Lett. **40**, 2017 (2013).
[28] P. A. Tsai, K. Riesing, and H. A. Stone, Density-driven convection enhanced by an inclined boundary: Implications for geological CO_2 storage, Phys. Rev. E **87**, 011003(R) (2013).
[29] R. E. Ecke and S. Backhaus, Plume dynamics in Hele-Shaw porous media convection, Phil. Trans. R. Soc., Ser. A **374**, 20150420 (2016).

[30] D. R. Hewitt, J. A. Neufeld, and J. R. Lister, Ultimate Regime of High Rayleigh Number Convection in a Porous Medium, Phys. Rev. Lett. **108**, 224503 (2012).
[31] J. Otero, L. A. Dontcheva, H. Johnston, R. A. Worthing, A. Kurganov, G. Petrova, and C. R. Doering, High-Rayleigh-number convection in a fluid-saturated porous layer, J. Fluid Mech. **500**, 263 (2004).
[32] O. Söhnel and P. Novotnỳ, *Densities of Aqueous Solutions of Inorganic Substances*, Vol. 22 (Elsevier, Amsterdam, Neth., 1985).
[33] J. E. Garcia, Fluid dynamics of carbon dioxide disposal into saline aquifers, Ph.D. dissertation, Lawrence Berkeley National Laboratory, 2003.
[34] J. Bear, *Dynamics of Fluids in Porous Media* (Elsevier, New York, 1972).
[35] See Supplemental Material at http://link.aps.org/supplemental/10.1103/PhysRevFluids.2.014102 for videos of the mixing dynamics of the density-driven convection.
[36] A. Riaz and Y. Cinar, Carbon dioxide sequestration in saline formations: Part I, review of the modeling of solubility trapping, J. Pet. Sci. Technol. **124**, 367 (2014).